Journal of Inorganic and Organometallic Polymers and Materials
https://doi.org/10.1007/s10904-021-02185-w

Effect of Cobalt and Nickel Doping on Structural and Magnetic Properties of Iron Oxide Nanoparticles

Imen Grabsi[1] · Faiza Bouaïcha[1,2] · Aicha Ziouche[3] · Nassima Bouaziz[1] · Mourad Zaabat[1] · Fikret Yildiz[4]

Received: 8 October 2021 / Accepted: 6 December 2021

Abstract
Two series samples of Iron Oxide nanoparticles doped with nickel and cobalt with different doping values (x = 0.01; 0.03; 0.05 and 0.07), were successfully synthesized by using sol–gel method, and then they were characterized by X-ray diffraction, scanning electron and vibrating sample magnetometer (VSM). X-ray diffraction analysis of two series samples showed the formation α-Fe_2O_3 nanoparticles, accompanied by two phases iron spinels, $CoFe_2O_4$ and $NiFe_2O_4$. In addition, the variations in grain size were observed for both two series. The observation by scanning electron microscopy reveals a change in the morphology of the grains of all the samples doped, which confirm the cobalt and nickel effect on the morphology of iron oxide nanoparticles. Magnetic measurements which were measured by VSM showed significant magnetic parameters such as coercivity and magnetization besides the ferromagnetic behavior of both two series doped with Cobalt and Nickel.

Keywords α-Fe_2O_3 sol–gel · $CoFe_2O_4$ · $NiFe_2O_4$ · Nanoparticles · Ferromagnetism

1 Introduction

The synthesis of nonmaterial's increases dramatically depending on different applications as catalysts, biological and electrical components [1–4]. We mention among them; iron oxides, including hematite (α-Fe_2O_3), which have attracted a lot of attention due to their important properties such as the lower band gap than an n-type semiconductor, in addition to its variable color and its high resistance to corrosion. Iron oxides have been used in various fields, such as pigments [5], medicine and human cells [6], corrosion [7], photoelectric chemical applications [8], catalysis [9], lithium-ion sensors and batteries [10]. In addition to this, several studies have been carried out, such as spheres and nano-particle flowers have been successfully prepared [11] by various techniques such as the hydrothermal process [12], the chemical precipitation mode [13] and the sol–gel method [14, 15].

Moreover, iron oxides associate with other elements of the periodic table forming a structure of phases iron spinels nanoparticles presented by the common formula AFe_2O_4 where (A = Mn, Fe, Co, Ni, Zn…) and are of great interest in magnetic materials, besides this, the interest of cobalt-iron applications are widening to biomedical applications [16] and hyperthermia [17], gas detection [18–20], lithium-ion batteries [21], catalytic studies [22], super capacitors [23] and solar cells [24]. Generally, the sol–gel method, to be a relatively a new industrial technology, due to its simplicity compared to the equipment used in other methods [25] and there are two methods, the first is called the colloidal method and the second is the polymeric route. The difference between them comes from the types of precursors used [14, 26].

The aim of the present study is to see the effect of cobalt and nickel as ferromagnetic doping on the structural, morphological and magnetic properties of hematite nanoparticles.

✉ Faiza Bouaïcha
bouaicha.faiza@yahoo.fr

1 Laboratory of the Active Components and Materials, University of Larbi Ben M'hidi, Oum El Bouaghi, Algeria

2 Physical Measurements Department, Institute of Science and Applied Techniques, Larbi Ben M'Hidi University, Oum El Bouaghi, Algeria

3 Research Centre in Industrial Technologies CRTI, Cheraga, Algeria

4 Physics Department, Gebze Technical University, 41400 Gebze, Kocaeli, Turkey

Published online: 11 January 2022

2 Experimental

All samples of α-Fe_2O_3 nanoparticles, doped with Co and Ni in different concentrations, were prepared by the sol–gel method. To prepare the undoped and doped solutions, we have used the following chemicals: 2 M Iron (III) Nitrate Nonahydrate [$Fe(NO_3)_3.9H_2O$], in addition to the Cobalt (II) Chloride Hexahydrate [$CoCl_2.6H_2O$] and Nickel (II) Acetate [$Ni(CH_3CO_2)_2.4H_2O$] as a precursor. All these preparations were dissolved in 8 ml of ethylene glycol ($C_2H_6O_2$) with the mixture stirred at 80 °C for 2 h, and then we have added 4.5 ml of NH_4OH to the solution for to get a homogeneous solution. Moreover, the gel has been dried and calcined at 150 °C during about 20 min. The resultant powders were then sintered at 800 °C for 2 h. After that, all samples are characterized by firstly X-ray diffraction patterns using BRUKER Discover D8 X-ray diffractometer with CoKα radiation ($\lambda_{CoK\alpha}$ = 1.7890 Å), where the identification of the existing phases were carried out using of HighScoreplus programme. Then Microphotographies observations were performed by a Zeiss Gemini SEM 300 Scanning Electron Microscope (SEM). Finally, magnetization measurements for all the samples, were performed using vibrating sample magnetometer Microsense VSM-09, where a magnetic field was applied from − 22 to 22 K Oe.

3 Results and Discussion

3.1 Structural Study

Figure 1 shows the XRD patterns of the undoped sample. The main reflections peaks observed at 2θ value of 28.09°, 38.68°, 41.58°, 47.79°, 58.09°, 63.68°, 68.02°, 73.94° and 75.87° attributed to Miller indices corresponding the diffraction planes (012), (104), (110), (113), (024), (116), (018), (214) and (300) respectively,

Corresponding to the α-Fe_2O_3 rhombohedral cell with the space group R3c, similar to the same one reported in ICDD card No. 00-033-0664 [9]. The refined cell parameters are a = 5.0356 Å, b = 5.0356 Å, c = 13.7489 Å. It should be noted that the complete absence of the impurity phases was observed, which indicated that the α-Fe_2O_3 phase are pure. The XRD patterns of the α-Fe_2O_3 samples doped with Co and Ni are shown in Figs. 2 and 3 respectively. The main peaks of the α-Fe_2O_3 phase are associated with the $CoFe_2O_4$ and $NiFe_2O_4$ phases, and belong to a cubic cell with space group Fd-3m similar to those mentioned in ICDD Card No. 00-022-1086 [18] and ICDD Card No. 2081-074-01 [27] respectively. Besides,

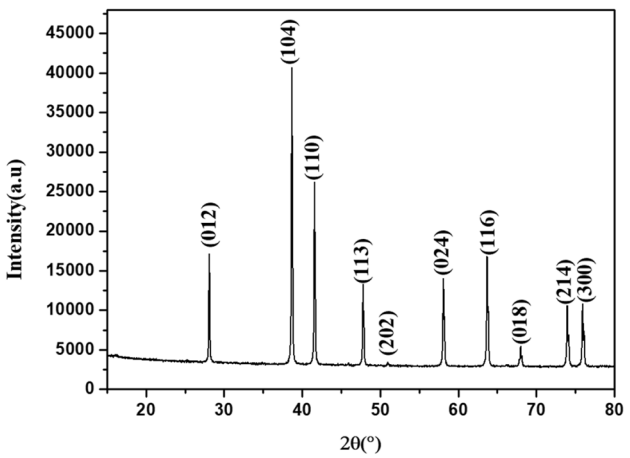

Fig. 1 XRD pattern of α-Fe_2O_3 undoped sample

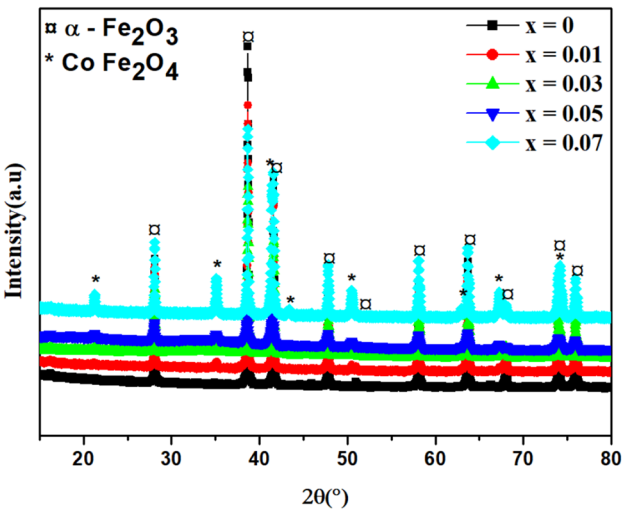

Fig. 2 XRD patterns of Cobalt doped α-Fe_2O_3 nanoparticles

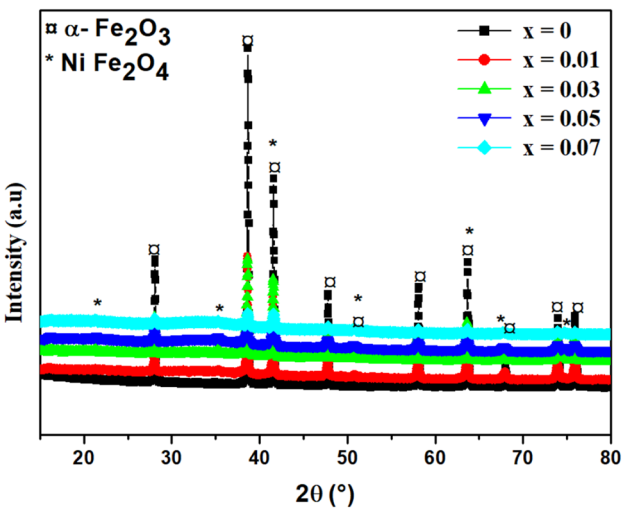

Fig. 3 XRD patterns of Nickel doped α-Fe_2O_3 nanoparticles

the successive decrease in intensity of the doped samples confirms the introduction of Co and Ni, in the pure phase. For all samples, we have observed the displacement of the peaks to the left with rate $2\theta = 0.03°$, for the concentrations of Co^{+2} and Ni^{+2} ions increased. This displacement is accompanied by a change of their intensity. As reported by Amit Kumar Rana et al. [28] and R. Krishnapriya [29], the doping by Co and Ni in the ZnO lattice induces a the displacement towards the higher 2θ angles. The authors attribute that to smaller ionic radius of the Co^{+2} (0.56 Å) and Ni^{+2} (0.55 Å) with respect to Zn^{+2} (0.60 Å), confirming that the Co^{+2} and Ni^{+2} ions are doped into the ZnO lattice. Our result seems then acceptable because the ionic radius of Fe^{+2} is (0.78 Å). In addition, these results are an indication of a change of the grain size.

The crystalline sizes of undoped and doped α-Fe_2O_3 phase have been estimated from the Scherer formula (1) [30] and listed in Table1:

Table 1 Crystallite size of different synthesized samples

	x = 0	x = 0.01	x = 0.03	x = 0.05	x = 0.07
Crystallite size of dopant (nm)					
Co	58,75	55,14	46,84	44,16	55,17
Ni		45,52	38,23	45,94	46,66

$$D = \frac{0.9\lambda}{\beta \cos\theta} \quad (1)$$

where D is the crystalline size, λ is the wavelength of X-ray where ($\lambda_{CoK\alpha} = 1.7890$ Å), β is the full width at half maximum (FWHM) and θ is the diffraction angle. The estimated result showed that the average crystallite size is 58.75 nm for the undoped α-Fe_2O_3 sample. But, when we introduced the Co or Ni atoms into the undoped phase, we notice a slight decrease in the size of the crystallites compared to the undoped sample, and it seems that there are a variation in the crystallites sizes of samples doped with Co and Ni, that go through the minimum, then increased slightly, when the sample are doped with x = 0.07 cobalt and x = 0.05 nickel. According to these result's saturation are noticed, when the doped are nickel.

Figures 4, 5, 6 shows SEM micrographs of undoped sample (α-Fe_2O_3) and Cobalt and Nickel doped samples respectively, with magnification at 5.04 KX in the secondary electron mode. It is clearly shown that the microstructure of the undoped sample is very different from that of the doped samples, in which the grains in the form of bacilli irregular [26], randomly oriented with 3 µm size. The porosity of this sample is important. Figure 5b1 shows the microstructure of the sample doped with cobalt (x = 0.01). The evolution of the nanoparticle morphology was observed from irregular to more regular shape. The grains have a flat shape with different size less than 2 µm and randomly oriented crystallites. In addition, the porosity of this sample has decreased compared

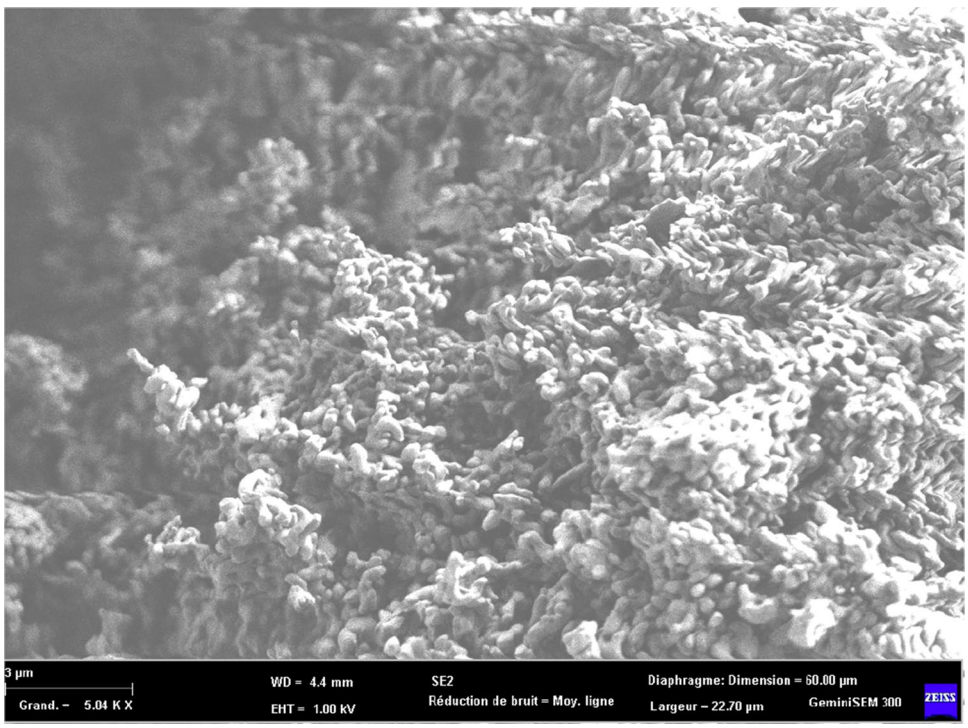

Fig. 4 SEM micrographs of sample undoped sample α-Fe_2O_3

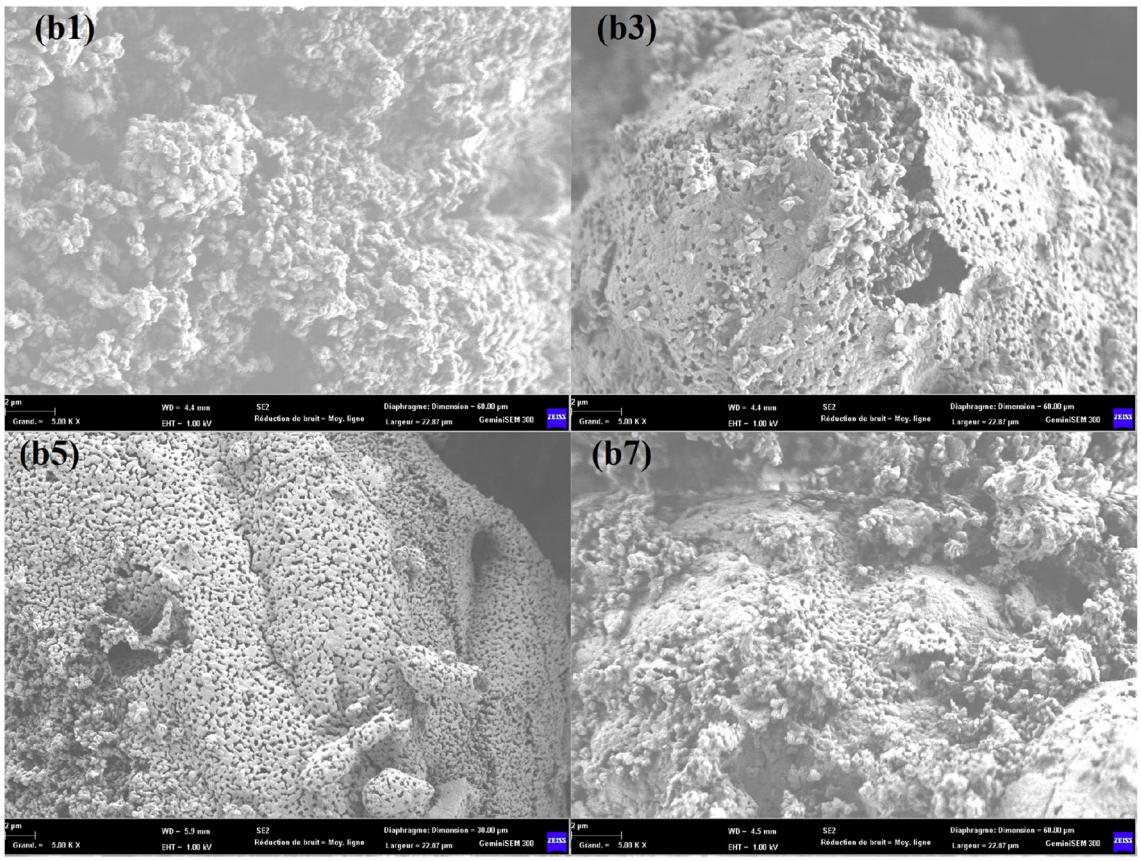

Fig. 5 SEM micrographs of samples doped with cobalt: **b1** x = 0.01, **b3** x = 0.03, **b5** x = 0.05 and **b7** x = 0.07

to the undoped sample. Then, for the doped samples with cobalt (x = 0.03; 0.05 and 0.07) respectively, the shape of the grains with different size less than 2 µm is changed compared to the undoped sample due to the presence of magnetic interaction resulting from the cobalt affected α-Fe_2O_3 nanoparticles [31], where the particles tend to agglomerate when doping increases. It is clearly visible from Fig. 6c1, c3, c5, c7, where we can see considerable change in morphology of the nanoparticle.The grains have a flat shape with different size less than 2 mm and randomly oriented crystallites. The pores which are visualized between these nanoparticles reveal a porous structure, which are preferred for gas detection applications [19, 20]. In addition, when the doping increases; the particles tend to accumulate, where induced the ferromagnetic behavior [32].

3.2 Magnetic Properties

Figures 7, 8 shows the plot of magnetization as a function of magnetic field (M–H curves) for different doped. The curves shows that both two series of samples have ferromagnetic behavior which attributed to doping effect [22, 28, 29, 33, 34]. However, as was evident from the hysteresis loop, the width of the loop increases when the nickel and cobalt doping concentration in the sample increases. The doping with cobalt considerably increases the coercive field and the magnets of saturation and residual, we also note an apparent saturation of saturation and residual magnets with the cobalt rate; with nickel the coercive field decreases considerably and the magnets of saturation and residual increases almost linearly with the nickel rate (Fig. 9). Table 2 summarizes the results of variable values of the coercivity, saturation of the magnetization and the residual magnetism who revel that for each sample, the values of the Ms and Mr depends on strongly the doping with Co and Ni, their increase was appearing considerably according to their increasing of each one of the doping elements. The coercive force decreases with increasing the nickel doping concentration, but in the case of the cobalt doping, reached a maximal value when the sample is doped with a rate x = 0.01. Beside, the Ms values increase significantly with increasing crystallite size, which has been confirmed by Jansi Rani et al. [33] and Srikrishna et al. [35]. Contrary to Srikrishna et al. [35] findings, Hc values decrease with increasing doping with cobalt. Doped With Co in the α-Fe_2O_3 structure causes the

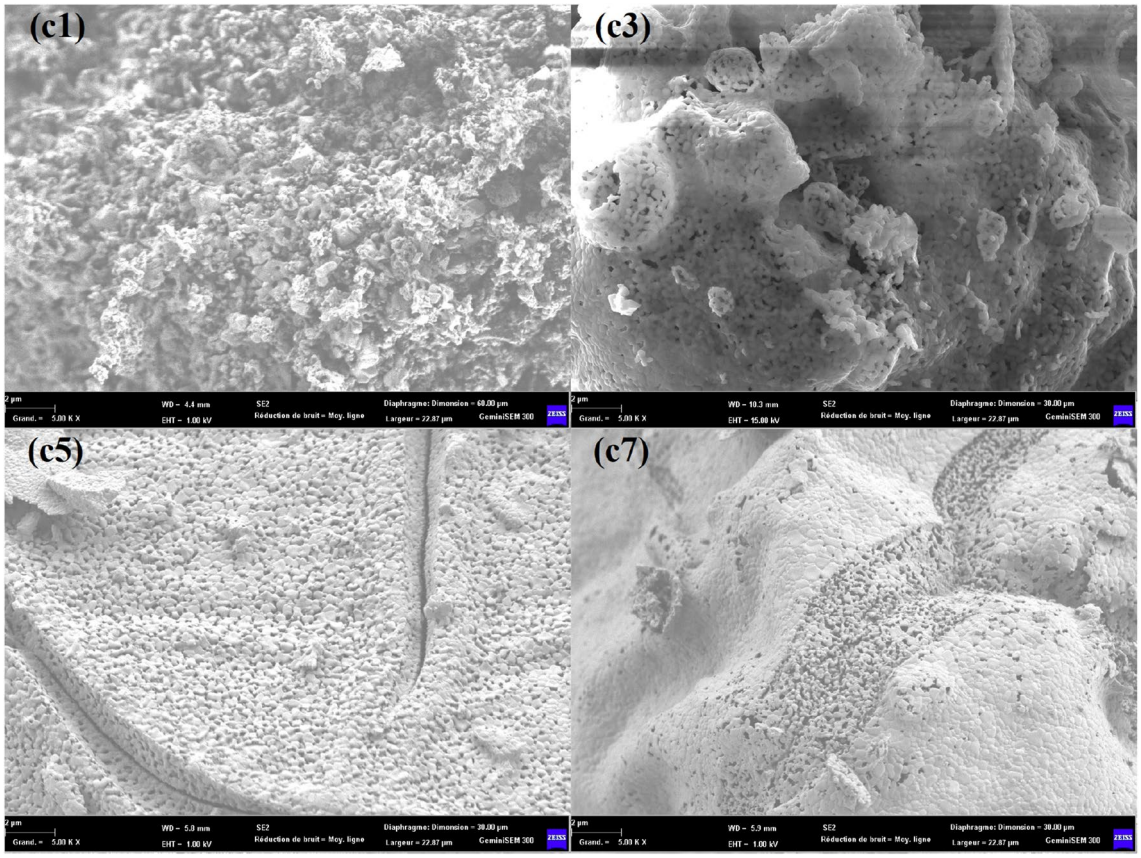

Fig. 6 SEM micrographs of samples doped with Nickel: **c1** x = 0.01, **c3** x = 0.03, **c5** x = 0.05 and **c7** x = 0.07

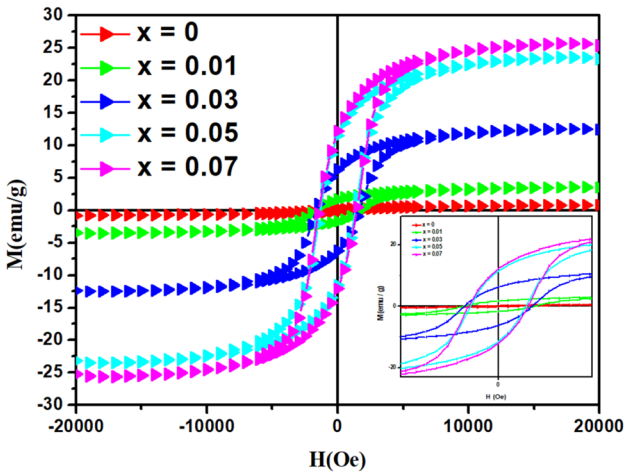

Fig. 7 M–H curves for Co-doped α-Fe_2O_3 nanoparticle

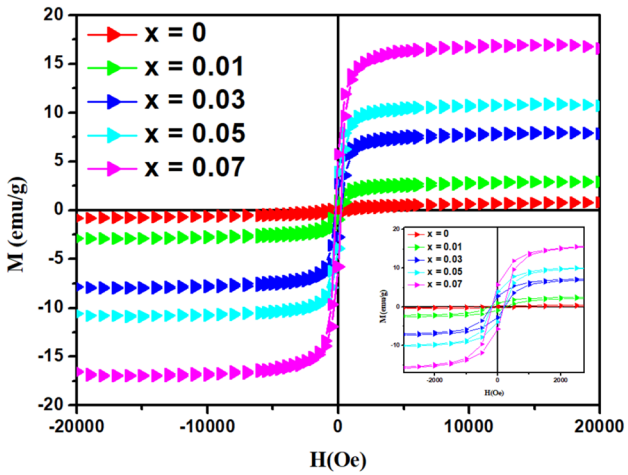

Fig. 8 M–H curves for Ni-doped α-Fe_2O_3 nanoparticles

occurrence of Co^{2+} in interstitial sites of oxygen, which leads to an increase in magnetic properties [36].

Figure 10 show the variation of the force field and the size of crystallite size. According to this representation, for the values between 0.01 and 0.07 of the samples doped with cobalt; the curve of the variation of the force field and the crystallites size, have the same change. The same change of the curve is seen when the doping with nickel, where the values between 0.01 and 0.03. This variation is linked to changes in the microstructure of the nanoparticle [30, 32]. However the boundary

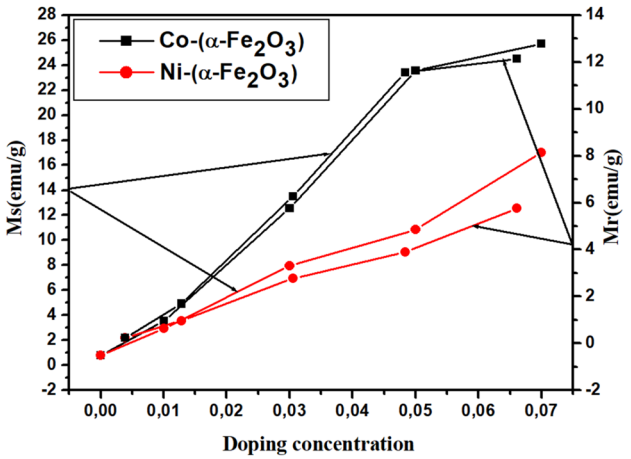

Fig. 9 The variation of saturation and residual magnetizations as a function of the doping rate

Table 2 Magnetic parameters of different synthesized samples

Dopant		Magnetic parameters		
		Hc (Oe)	Ms (emu/g)	Mr (emu/g)
α-Fe_2O_3	x = 0	1087.12	805.737 E^{-3}	232.421 E^{-3}
Co	x = 0.01	1741.64	3.527	1.692
	x = 0.03	1652.90	12.545	6.270
	x = 0.05	1337.22	23.566	11.539
	x = 0.07	1455.24	25.684	12.139
Ni	x = 0.01	265.92	2.927	967.093 E^{-3}
	x = 0.03	217.92	7.964	2.775
	x = 0.05	192.24	10.855	3.899
	x = 0.07	186.70	17.005	5.750

of Hc is influenced by the particle sizes and the homogeneity of each material [22]. Table 3 shows a simple comparison between the values previously studied, and obtained in our study. For the undoped sample (α-Fe_2O_3) and doped sample with cobalt ($CoFe_2O_4$), the Hc values are bigger than those mentioned by Qasim et al. [16], and Srikrishna et al. [35]. For sample doped with nickel ($NiFe_2O_4$), were the Hc values are improved compared to the values reported in the literature [27, 33, 34]. The magnetization can be influenced by the calcinations temperature [37], and this by controlling the morphology of the nanoparticle [38], which was confirmed by Pottker et al. [34]. For doped samples with nickel, the Ms values, are close to the values reported in the literature [33, 34], and increase with increasing the doped.

4 Conclusions

In this work, we are presented elaboration and characterizations of two a series of the α-Fe_2O_3 nanoparticle doped with cobalt and nickel. At low concentration, Cobalt and Nickel doping in α-Fe_2O_3 nanoparticle phase does not change significantly the crystallographic structure of the samples. The grain of crystallites size decreases with increasing doping. The doping also affects the microstructure of the undoped sample α-Fe_2O_3 and doped ($CoFe_2O_4$ and $NiFe_2O_4$). Magnetic measurements which were measured by the VSM showed important magnetic parameters such as coercivity and magnetization, as well as the magnetic behavior of both two series.

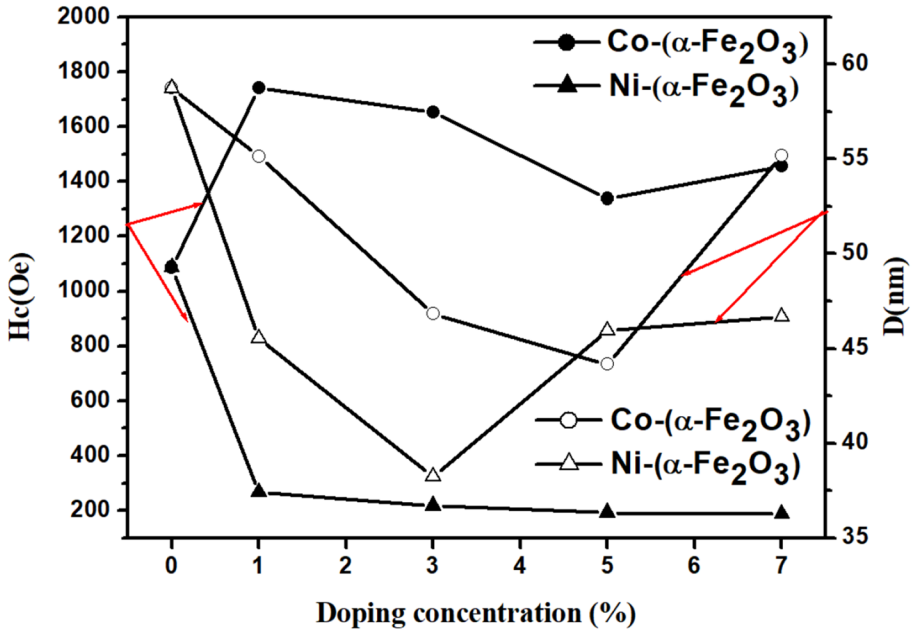

Fig. 10 Graphical representation of the dependence of coercif field and crystallite size

Table 3 Comparison of Hc and Ms Values, between literature and our work

Samples	Hc (Oe)	Ms (emu/g)	Ref.
α-Fe_2O_3	1087.12	805.737 E^{-3}	This work
	2340	0.53	[33]
	3891	0.4193	[26]
	362	1.861	[34]
1% Co–(α-Fe_2O_3)	1741.64	3.527	This work
	362	5.481	[34]
7% Co–(α-Fe_2O_3)	1455.24	25.684	This work
	362	12.6118	[34]
1% Ni–(α-Fe_2O_3)	265.92	2.927	This work
7% Ni–(α-Fe_2O_3)	186.70	17.005	
Co Fe_2O_4	230–240	88	[16]
	9900–17700	51–66	[35]
Ni Fe_2O_4	40–160	42–53	[27]
	118.4	12.1	[32]
	25.3	16.71	[30]

References

1. C.D. Powell, A.J. Atkinson, Y. Ma, M. Marcos-Hernandez, D. Villagran, P. Westerhoff, M.S. Wong, J. Nanopart. Res. **2**, 22–48 (2020). https://doi.org/10.1007/s11051-020-4770-4
2. N. Pariona, M. Herrera-Trejo, J. Oliva, A.I. Martinez, J. Nanomater. **2016**, 3427809 (2016). https://doi.org/10.1155/2016/3427809
3. C. Karunakaran, S. SakthiRaadha, P. Gomathisankar, P. Vinayagamoorthy, Powder Technol. **60**, 487–499 (2013). https://doi.org/10.1016/j.powtec.2013.06.011
4. F. Mueller, D. Bresser, V.S.K. Chakravadhanula, S. Passerini, J. Power Sources **299**, 398–402 (2015). https://doi.org/10.1016/j.jpowsour.2015.08.018
5. H. Katsuki, S. Komarneni, J. Am. Ceram. Soc. **86**, 183–185 (2003). https://doi.org/10.1111/j.1151-2916.2003.tb03300.x
6. R. Kumar, S. Shampa, G. Suja, S. Lakshmana Senthil, T.V. Kumar, Colloids Surf. B. **157**, 101–109 (2017). https://doi.org/10.1016/j.colsurfb.2017.05.052
7. K. Kamburova, V. Milkova, Ts. Radeva, Colloids Surf. A. **462**, 237–243 (2014). https://doi.org/10.1016/j.colsurfa.2014.09.018
8. H. Jingwei, H. Guowen, D. Yong, P. Mingchun, M. Baochun, J. Catal. **340**, 261–269 (2016). https://doi.org/10.1016/j.jcat.2016.05.007
9. W. Dechao, J. Lijun, L. Yang, H. Haoquan, Fuel **210**, 803–810 (2017). https://doi.org/10.1016/j.fuel.2017.09.008
10. C. By Jun, X. Lina, L. Weiyang, G. Xinglong, Adv. Mater. **17**, 582–586 (2005). https://doi.org/10.1002/adma.200401101
11. C. Chang-Yan, Q. Jin, Y. Wen-Sheng, Z. Jun-Fa, W. Zi-Yu, S. Wei-Guo, Am. Chem. Soc. Langmuir **28**, 4573–4579 (2012). https://doi.org/10.1021/la300097y
12. K. Munawar, Y. Jianjia, L. Ning, L.L. Robert, J. Nanopart. Res. **16**, 23–62 (2014). https://doi.org/10.1007/s11051-014-2362-x
13. A. Lassoued, B. Dkhil, A. Gadri, S. Ammar, Results Phys. **7**, 3007–3015 (2017). https://doi.org/10.1016/j.rinp.2017.07.066
14. T.K. Kundu, M. Mukherjee, D. Chakravorty, J. Mater. Sci. **33**, 1759–1763 (1998). https://doi.org/10.1023/A:1004376515384
15. C. Baratto, P.P. Lottici, D. Bersani, G. Antonioli, G. Gnappi, A. Montener, J. Sol-Gel. Sci. Technol. **13**, 667–671 (1998). https://doi.org/10.1023/A:1008694519106
16. M. Qasim, K. Asghar, D. Das, Ceram. Int. **45**, 24971–24981 (2019). https://doi.org/10.1016/j.ceramint.2019.04.049
17. S. Munjal, N. Khare, B. Sivakumar, D. Nair Sakthikumar, J. Magnet. Magnet. Mater. **477**, 388–395 (2019). https://doi.org/10.1016/j.jmmm.2018.09.007
18. H.J. Zhang, L.Z. Liu, X.R. Zhang, S. Zhang, F.N. Meng, J. Alloy. Compd. **788**, 1103–1112 (2019). https://doi.org/10.1016/j.jallcom.2019.03.009
19. S. Zhang, W. Jiang, Y. Li, X. Yang, P. Sun, F. Liu, X. Yan, Y. Gao, X. Liang, J. Ma, G. Lu, Sensors Actuators B **291**, 266–274 (2019). https://doi.org/10.1016/j.snb.2019.04.090
20. J.Y. Patil, D.Y. Nadargi, J.L. Gurav, I.S. Mulla, S.S. Suryavanshi, Mater. Lett. **124**, 144–147 (2014). https://doi.org/10.1016/j.matlet.2014.03.051
21. G. Karunakaran, M. Kundu, G. Maduraiveeran, E. Kolesnikov, M.V. Gorshenkov, S.K. Balasingam, S. Kumari, M. Sasidharan, D. Kuznetsov, Microporous Mesoporous Mater. **272**, 1–7 (2018). https://doi.org/10.1016/j.micromeso.2018.06.005
22. K. Kombaiah, J.J. Vijaya, L.J. Kennedy, K. Kaviyarasu, Mater. Chem. Phys. **221**, 11–28 (2019). https://doi.org/10.1016/j.matchemphys.2018.09.012
23. X. Gao, W. Wang, J. Bi, Y. Chen, X. Hao, X. Sun, J. Zhang, Electrochim. Acta **296**, 181–189 (2019). https://doi.org/10.1016/j.electacta.2018.11.054
24. G. Ying, L. Tao, W. Ning, L. Qiang, L. Hong, L. Jianbao, J. Qinglong, W. Lili, G. Zhanhu, Nano Energy **38**, 193–200 (2017). https://doi.org/10.1016/j.nanoen.2017.05.026
25. S. Das, M.J. Hendry, J. Nanopart. Res. **16**, 25–35 (2014). https://doi.org/10.1007/s11051-014-2535-7
26. K. Raja, M. Mary Jaculine, M. Jose, S. Verma, A.A.M. Prince, K. Ilangovan, K. Sethusankar, S. Jerome Das, Superlattices Microstruct. **86**, 306–312 (2015). https://doi.org/10.1016/j.spmi.2015.07.044
27. D.K. Dinkar, B. Das, R. Gopalan, B.S. Dehiya, Mater. Chem. Phys. **218**, 70–76 (2018). https://doi.org/10.1016/j.matchemphys.2018.07.020
28. R. Krishnapriya, S. Praneetha, S. Kannan, A. Vadivel Murugan, ACS Sustain. Chem. Eng. **5**, 9981–9992 (2017)
29. A. Kumar Rana, Y. Kumar, P. Rajput, S.N. Jha, D. Bhattacharyya, P.M. Shirage, ACS Appl. Mater. Interf. **9**(8), 7691–7700 (2017)
30. H.P. Klug, L.E. Alexander, *X-ray diffraction procedures: for polycrystalline and amorphous materials, 2nd edition*, vol. 32 (Wiley, Hoboken, 1974), pp. 992–999
31. M. Kamranifar, A. Allahresani, A. Naghizadeh, J. Hazard. Mater. **366**, 545–555 (2019). https://doi.org/10.1016/j.jhazmat.2018.12.046
32. Y. Slimani, M.A. Almessiere, M. Nawaz, A. Baykal, S. Akhtar, I. Ercan, I. Belenli, Ceram. Int. **45**, 6021–6029 (2019). https://doi.org/10.1016/j.ceramint.2018.12.072
33. B. Jansi Rani, M. Ravina, B. Saravanakumar, G. Ravi, V. Ganesh, S. Ravichandran, R. Yuvakkumar, Nano-Structures Nano-Objects. **14**, 84–91 (2018). https://doi.org/10.1016/j.nanoso.2018.01.012
34. W.E. Pottker, R. Ono, M.A. Cobos, A. Hernando, J.F.D.F. Araujo, A.C.O. Bruno, S.A. Lourenço, E. Longo, F.A. La Porta, Ceram. Int. **44**, 17290–17297 (2018). https://doi.org/10.1016/j.ceramint.2018.06.190
35. M. Tadic, L. Kopanja, M. Panjan, S. Kralj, J. Nikodinovic-Runic, Z. Stojanovic, Appl. Surf. Sci. **320**, 183–187 (2014). https://doi.org/10.1016/j.apsusc.2017.01.115
36. S.I. Srikrishna Ramya, C.K. Mahadevan, J. Solid State Chem. **211**, 37–50 (2014). https://doi.org/10.1016/j.jssc.2013.11.022

37. B. Purnama, A.T. Wijayanta, Suharyana, J. King Saud. Univ. Sci. **31**, 956–960 (2018). https://doi.org/10.1016/j.jksus.2018.07.019
38. M. Tadic, M. Panjan, V. Damnjanovic, I. Milosevic, Appl. Surf. Sci. **320**, 183–187 (2014). https://doi.org/10.1016/j.apsusc.2014.08.193